Lattice Deformation at Submicron Scale: X-Ray Nanobeam Measurements of Elastic Strain in Electron Shuttling Devices

C. Corley-Wiciak [1,*] M.H. Zoellner [1] I. Zaitsev [1] K. Anand [1] E. Zatterin [2] Y. Yamamoto [1]
A.A. Corley-Wiciak [1,3] F. Reichmann [1] W. Langheinrich [4] L.R. Schreiber [5] C.L. Manganelli [1]
M. Virgilio [6] C. Richter [7,†] and G. Capellini [1,8]

[1] *IHP – Leibniz-Institut für innovative Mikroelektronik, Im Technologiepark 25, D-15236 Frankfurt(Oder), Germany*

[2] *ESRF - European Synchrotron Radiation Facility, X-ray Nanoprobe Group, 71, Avenue des Martyrs, CS 40220, 38043 Grenoble Cedex 9, France*

[3] *RWTH Aachen University, Aachen, Germany*

[4] *Infineon Technologies Dresden GmbH und Co.KG, Dresden, Germany*

[5] *JARA-FIT Institute for Quantum Information, Forschungszentrum Jülich and RWTH Aachen University, Aachen, Germany*

[6] *Department of Physics Enrico Fermi, Università di Pisa, Pisa 56126, Italy*

[7] *IKZ – Leibniz -Institut für Kristallzüchtung, Max-Born-Straße 2, D-12489 Berlin, Germany*

[8] *Dipartimento di Scienze, Universita Roma Tre, Viale G. Marconi 446, Roma 00146, Italy*

The lattice strain induced by metallic electrodes can impair the functionality of advanced quantum devices operating with electron or hole spins. Here, we investigate the deformation induced by CMOS-manufactured titanium nitride electrodes on the lattice of a buried 10-nm-thick $Si/Si_{0.66}Ge_{0.34}$ quantum well by means of nanobeam scanning x-ray diffraction microscopy. We are able to measure TiN-electrode-induced local modulations of the strain tensor components in the range of $2–8 \times 10^{-4}$ with about 60-nm lateral resolution. We evaluate that these strain fluctuations are reflected in local modulations of the potential of the Si conduction-band minimum larger than 2 meV, which is close to the orbital energy of an electrostatic quantum dot. We observe that the sign of the strain modulations at a given depth of the quantum-well layer depends on the lateral dimensions of the electrodes. Since our work explores the impact of device geometry on the strain-induced energy landscape, it enables further optimization of the design of scaled CMOS-processed quantum devices.

I. INTRODUCTION

The characterization of mechanical strain at the nanometer scale is essential for improving the homogeneity and electronic performance in advanced semiconductor-based electronic devices [1,2]. In particular, it is of paramount importance to assess the impact of the fabrication processes on the mechanical stress generated by electrodes made from metals or metallic compounds [3]. Indeed, an electrode exerts a stress onto the underlying and neighboring semiconductor layers, thus inducing local lattice deformations, which are described by the spatially dependent strain tensor, $\varepsilon(x, y, z)$. In turn, the lattice strain affects electronic properties such as charge-carrier mobility [4], band-edge potential [5], and tunnel couplings [2].

This is particularly relevant for modern semiconductor-based quantum devices, such as qubits, which are still exceedingly difficult to fabricate in large numbers and require a high degree of homogeneity in their material environment [6]. Spin qubits housed in electrostatic quantum dots (QDs) are under the spotlight, since their fabrication can be integrated with microelectronics foundry environments [7,8], leveraging the high maturity level of Si-based complementary metal oxide semiconductor (CMOS) processes [9]. For this purpose, commonly used metals for manufacturing electrodes in small-scale device processing, such as Al, Pd, and Pt [10–12], should be replaced by materials commonly used in CMOS foundries, such as titanium nitride (TiN) [13], which has the

*corley@ihp-microelectronics.com
†carsten.richter@ikz-berlin.de

advantage of being a thermally stable and chemically mostly inert material with low resistance, and moreover, it acts as a diffusion barrier [14,15].

Quantum processors based on electrostatic QDs rely on gate electrodes, thus this choice of material is particularly relevant with regard to their spatial homogeneity. As a matter of fact, the realization of large arrays of densely packed QDs is required in architectures allowing for error-correction schemes [16]. Each error-corrected logical qubit would involve operating thousands of physical qubits [17]. Long coherence times are already demonstrated for electron spins housed in epitaxial $Si/Si_{0.7}Ge_{0.3}$ heterostructures [18], and the simultaneous operation of multiple semiconductor spin qubits has recently been reported [19]. The operation of qubits in large arrays requires spin-coherent communication pathways among them [20,21], which can be realized, e.g., by means of the quantum bus (qubus) architecture. A qubus device, as depicted in Fig. 1(a), shuttles electrons in a conveyor-mode scheme using a propagating sinusoidal potential pulse. This is generated by modulating the voltages on an array of "clavier" electrodes [12,22]. Shuttling takes place either by adiabatic Landau-Zener transitions across an array of tunnel-coupled QDs or by adiabatic motion of a quantum dot, as described in detail by Seidler *et al.* [12]. As shown in Fig. 1(b), clavier-gate arrays can also be employed to establish several QDs that may contain single-spin qubits [10].
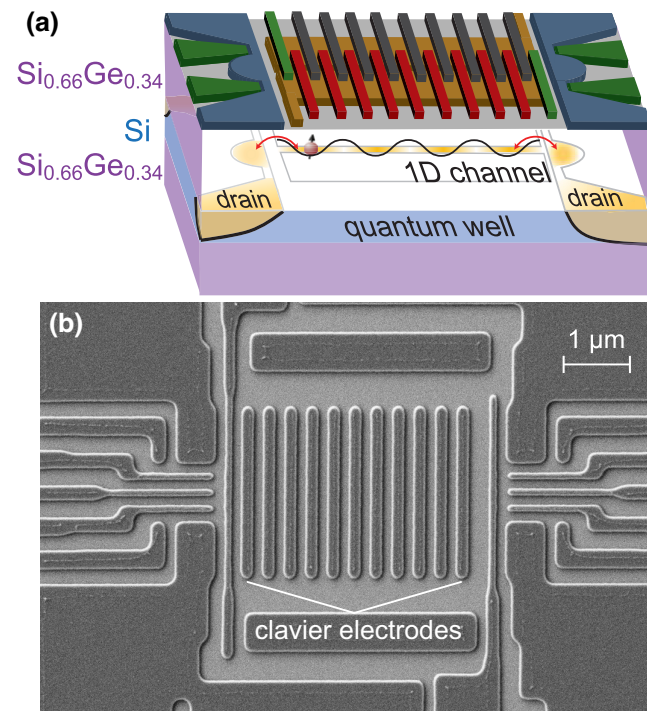
The operation of several physical qubits and their interconnection by the qubus requires a control scheme with voltages shared between the electrodes [20]; this does not allow for retuning of individual QDs. Therefore, the potential landscape in the active region of the device must feature a high degree of spatial homogeneity. Thus, among other things, local mechanical deformations in the lattice caused by the electrodes should be controlled and experimentally verified, due to their impact on the band-edge potential [6,23,24].

In general, the internal stress of a metal-compound thin film (or stripe) is comprised of thermomechanical and residual stress [25]. The thermomechanical stress is generated by the mismatch of the coefficient of thermal expansion (CTE) between the material and the semiconductor-oxide virtual substrate (VS) when the sample cools down from deposition to the operation temperature [2]. The residual stress is accumulated during the deposition process owing to variations in crystallite sizes, orientations, relaxations, and coalescence [25]. In particular, stress exerted from TiN thin films on Si or $Si_{1-x}Ge_x/Si$ substrates may be tuned from tensile to compressive [26, 27], by acting on layer thickness and deposition-process parameters [3,28]. This allows the deposition process to be tuned towards targeted stress values for specific applications.

The stress within large TiN films is typically investigated by wafer-curvature measurements [29]; however, the stress in small lithographically fabricated electrodes may differ from the unstructured film due to amorphization, oxidation, and plastic relaxation occurring during structuring. From this perspective, scanning measurements with focused x-ray beams are well suited to study the local material properties in microelectronic devices [30,31].

Motivated by the above considerations, we employ scanning x-ray diffraction microscopy (SXDM) at the x-ray nanoprobe beamline ID01/ESRF [32,33] to obtain microscopic maps of the lattice strains induced by TiN electrodes deposited on the top surface of two samples with 10-nm-thick Si quantum wells (QWs) grown on $Si_{0.66}Ge_{0.34}$ buffers on Si(001) substrates. More precisely, we compare the local strain distribution measured in two devices sharing the same epitaxial layer stack and device layout, but differing in the sputtering process used for TiN deposition, resulting in different global stresses in the TiN layer.

To evaluate the impact of the strain fluctuations on the potential landscape of the QW, using the measured strain profiles, we calculate the local perturbation of the Si conduction-band edge in the framework of deformation-potential theory [34]. Furthermore, we employ finite-element-method (FEM) simulations with COMSOL Multiphysics to investigate the strain-field geometry induced by electrodes of varying lateral dimensions in the underlying active layer.

FIG. 1. (a) Schematic cross section of a qubus device; reproduced with permission [22]. (b) Top-view SEM image around the clavier electrodes.

II. EXPERIMENT

The epitaxial layer stack of the samples, as shown in Fig. 2(a), was grown on a commercial 200-mm Si wafer by reduced-pressure chemical vapor deposition (CVD) and is comprised of five 500-nm-thick step-graded $Si_{1-x}Ge_x$ layers with increasing Ge content x, a 4-μm-thick plastically relaxed $Si_{0.66}Ge_{0.34}$ buffer, a 10-nm pseudomorphic Si QW layer, a 30-nm $Si_{0.66}Ge_{0.34}$ barrier, and a sacrificial Si cap (<2 nm). The threading dislocation density was measured to be $<2 \times 10^6$ cm^{-2} by pit counting after a Secco etch. After removing the cap layer for surface cleaning, a 10-nm SiO_2 dielectric layer was deposited on top of the semiconductor stack by CVD. Finally, a TiN film of approximately 30 nm thickness was deposited by sputtering physical vapor deposition (PVD), followed by deposition of a SiO_2 hard mask used to fabricate the metal-gate stripes by UV lithography.

Two samples, A and B, are studied in this work. Sample A was sputtered with a magnetron for a denser plasma, while sample B was sputtered without the magnetron. The average global stress the TiN was subjected to was determined by measuring the curvature of the samples by x-ray diffraction (XRD) after processing and applying Stoney's equation [29,35]. We found a stronger stress for sample A ($\sigma_A = -2.6$ GPa) and a weaker stress for sample B ($\sigma_B = -1.5$ GPa).

The synchrotron measurements were carried out at ID01/ESRF with the setup depicted in Fig. 2(b). The x-ray beam was focused by a Fresnel zone plate (FZP) to a spot of about 60 nm in diameter on the sample surface, while higher-order diffraction from the FZP was blocked by an order-sorting aperture. The spot size was verified by ptychographic reconstruction [35,36]. The x-ray energy was set to 10 keV, at which the 335 reflection of Si was accessible at near-normal incidence and grazing exit of the x-ray beam. The high incidence angle of approximately 88° avoids any significant broadening of the beam footprint by projection on the sample surface, while the small exit angle of approximately 8° ensures a shallow penetration depth of the x-rays, and thus, high sensitivity to the QW layer close to the sample surface. Simultaneously with diffraction, fluorescence from the Ti K edge is mapped with an energy-resolved x-ray detector, allowing tracking of the TiN electrodes.

The experimental maps were acquired by scanning the sample in steps of about 50 nm across the x-ray beam with a piezo stage, while the diffraction signal was recorded with a Maxipix area detector. Due to the improved brilliance after the extremely bright source upgrade [37], an exposure time of 20 ms per spot on the sample was sufficient to measure the 10-nm-thick QW-layer diffraction signal with a signal-to-noise ratio of >10. To sample a three-dimensional (3D) volume of reciprocal space, diffraction maps were measured for a series of sample rocking angles, ω. In this way, from the diffraction patterns measured at every spot on the sample, maps of the local scattering vector were generated (see the Supplemental Material for details [35]).

Measurement of an SXDM dataset for one Bragg reflection took about 6 h, including alignment overhead. Thus, the total data acquisition time per sample was about 18 h. No systematic degradation of the diffraction or fluorescence signal from the Si or $Si_{0.66}Ge_{0.34}$ layers was observed throughout the measurement.

III. RESULTS

An exemplary 3D reciprocal space map (RSM) for one spot on the sample is shown in Fig. 2(c). The most intense
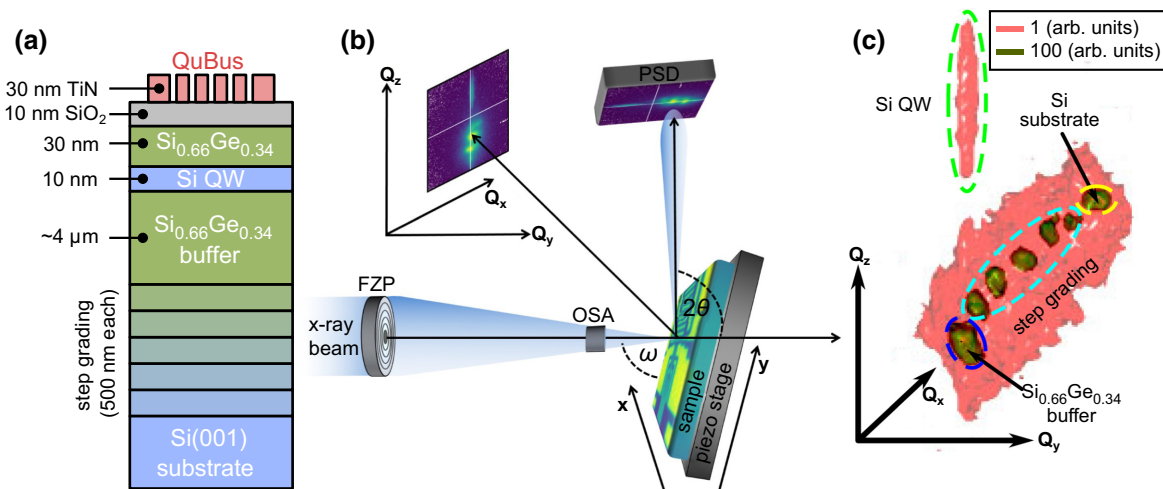

FIG. 2. (a) Heterostructure layer stack of samples. (b) Experimental setup of the SXDM measurement. (c) Isosurface plot of the 3D RSM around the 335 Bragg reflections of the heterostructure for one spot on the sample. Axes of reciprocal space are defined as $\mathbf{Q_x}$|| [1$\bar{1}$0], $\mathbf{Q_y}$|| [110]], and $\mathbf{Q_z}$||[001].

peaks in the RSM originate from the Si substrate and the 4-μm-thick buffer layer with constant composition. Between them, five intensity peaks can be observed, stemming from the discrete composition steps of the graded buffer material. The signal Bragg peak corresponding to the Si QW is located above the $Si_{0.66}Ge_{0.34}$ signal, at equal in-plane momentum transfers $\mathbf{Q_x}$, $\mathbf{Q_y}$, meaning that the QW is pseudomorphic to the buffer layer. Remarkably, the QW signal can be clearly separated from the more intense signals of the buffer along $\mathbf{Q_z}$ due to its smaller out-of-plane lattice constant.

We note that, in our reference system, the orientation of the length constants of the unit cell, the planes of the direct and reciprocal lattice and coordinates of the maps is defined as: $a||\mathbf{x}||\mathbf{Q_x}||[1\bar{1}0]$, $b||\mathbf{y}||\mathbf{Q_y}||[110]$, $c||\mathbf{z}|\,|\mathbf{Q_z}||\,[001]$.

By combining diffraction maps of the 335 and $\bar{3}\bar{3}5$ Bragg reflections, we can measure the lattice constants b and c and the angle, α, of the Bravais cell in the Si QW [38]. These data are used to generate maps in the direct space of the ε_{yy}, ε_{zz}, and ε_{yz} components of the lattice strain tensor, ε, by relying on the following equations [39]:

$$\varepsilon_{yy} = \frac{b \sin \alpha}{a_{Si}} - 1, \tag{1}$$

$$\varepsilon_{zz} = \frac{c}{a_{Si}} - 1, \tag{2}$$

$$\varepsilon_{yz} = \frac{1}{2} \frac{b \cos \alpha}{a_{Si}} \tag{3}$$

where a_{Si} was set to a value of 5.4309 Å [40]. With a diffraction map of the $3\bar{3}5$ reflection, we also determine the local value of QW lattice constant a, and corresponding strain ε_{xx} in the small-angle approximation as

$$\varepsilon_{xx} = \frac{a}{a_{Si}} - 1. \tag{4}$$

In Fig. 3, maps of the Ti K-edge x-ray fluorescence, f, and four components of the strain tensor are shown for "high-stress" sample A (top row) and "low-stress" sample B (bottom row). The fluorescence is given in counts per second; the strain is dimensionless and given in percent. The maps cover slightly different areas of the qubus on the two samples due to sample drift during the measurement (~1 μm total), which is caused by thermal settling and a residual offset between the beam focus and the ω-rotation axis. This drift is tracked during the measurement by simultaneously observing the diffraction and fluorescence signals [Figs. 3(a) and 3(b)]. The orientation of the coordinate system with respect to the crystallographic axes is specified in the inset of Fig. 3(a).

From the symmetric in-plane strain components, we measure in the pseudomorphic Si QW a biaxial global average strain, corresponding to $\varepsilon_{xx} \approx \varepsilon_{yy} \approx 1.3\%$, as expected from the lattice mismatch between Si and the $Si_{0.66}Ge_{0.34}$ virtual substrate.

With respect to this average biaxial strain, in both datasets, we observe a spatial distribution of the lattice
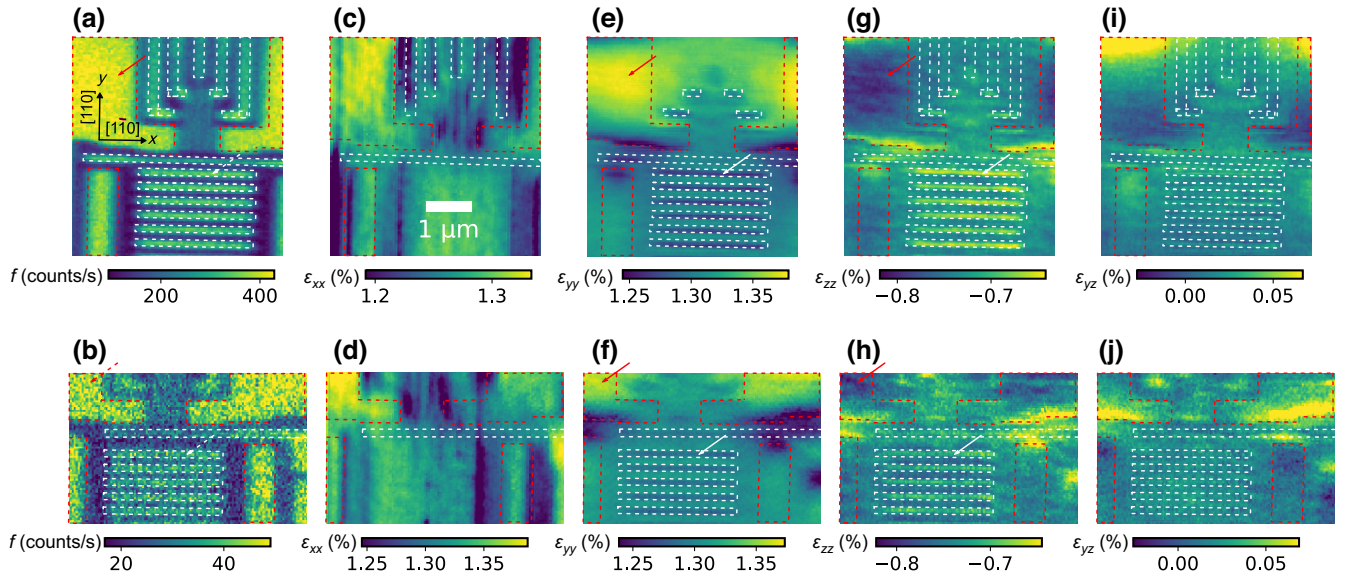

FIG. 3.   SXDM maps of samples A (top row) and B (bottom row). Black arrows describe the orientation of the crystallographic axes; scale is identical for all images. Clavier electrodes are located in the bottom region of the maps. Maps of (a),(b) Ti K-edge fluorescence, f, and strains in the Si QW layer: (c),(d) ε_{xx}, (e),(f) ε_{yy}, (g),(h) ε_{zz}, (i),(j) ε_{yz}. Device geometry is outlined by dotted lines, with contact pads of large lateral width marked in red and narrow electrodes in white. Notice that orientation of the $(1\bar{1}0)$ and (110) lattice planes is consistent with the observed direction of misfit-dislocation (MD) bunches in strain maps for the relaxed $Si_{0.66}Ge_{0.34}$ buffer shown in the Supplemental Material [35].

strain in the QW layer in the form of a "footprint" of the device, as evidenced by the dashed lines. By comparing the fluorescence maps for both samples to the strain maps, it is apparent that this strain modulation in the QW layer is due to the overlying TiN device.

We point out that there is a pronounced difference between the effect on the strain in the QW brought by either wide pads (red arrows) or narrow electrodes (white arrows). Indeed, underneath the wide structures, there is a tensile modulation of the in-plane lattice strains ε_{xx} [Figs. 3(c) and 3(d)] and ε_{yy} [Figs. 3(e) and 3(f)], while under narrow TiN stripes, in particular the clavier electrodes outlined by the white dashed boxes, the in-plane strain modulation becomes compressive, mainly due to smaller values of the diagonal strain component, which corresponds to the direction orthogonal to the electrode axis. Thus, the lateral dimensions of the lithographic structures appear to determine not just the magnitude, but also the quality of their effect on the lattice strain in the underlying layer.

In the qubus, electrons are shuttled through the clavier electrodes. Thus, lattice deformation underneath them is most important for the device, and hence, in the following we focus on this region of the device.

In line with the above observations, the symmetric in-plane strain component, ε_{xx} [Figs. 3(c) and 3(d)], appears to be practically unaffected by the clavier electrodes that run along the [1$\bar{1}$0] direction. However, across TiN stripes oriented along the [110] direction, we observe characteristic modulations in ε_{xx} of several 10^{-4}. Accordingly, the clavier electrodes have a compressive effect on ε_{yy}, with a total bandwidth of about 4×10^{-4} for sample A [Fig. 3(e)] and about 2×10^{-4} for sample B [Fig. 3(f)]. This modulation is noticeably homogeneous both along each stripe and across different electrodes.

For the out-of-plane strain component, which has an average value of $\varepsilon_{zz} \approx -0.73\%$, we also observe effects stemming from the TiN structures, but with reversed sign compared to the modulations of the in-plane strains: When the Si crystal lattice is strained along an in-plane direction by an electrode, it reacts in the vertical direction, since it tends to preserve the volume. Thus, we observe that ε_{zz} becomes more positive underneath the clavier electrodes, with modulations of up to about 8×10^{-4} for sample A [Fig. 3(g)] and up to about 4×10^{-4} for sample B [Fig. 3(h)].

The average value of the off-diagonal strain component, ε_{yz}, is close to zero, as expected for the case of a purely biaxial distortion, but there are local modulations connected to the truncation of the electrodes. Thus, the shape of the device is also well recognizable in the ε_{yz} maps [Figs. 3(i) and 3(j)]. They show modulations across the clavier electrodes of a magnitude of approximately 2×10^{-4}, thus clearly demonstrating a shear deformation of the lattice in the y-z plane.

Leveraging on the relationship,

$$\nu = \frac{1}{1 - (\varepsilon_{xx} + \varepsilon_{yy})/\varepsilon_{zz}} \approx \frac{1}{1 + (C_{33}/C_{13})}, \quad (5)$$

which links the lattice strains, all measured by SXDM, to the Poisson number, ν, and the elastic coefficients, $C_{13} = C_{23}$ and C_{33} [41,42], we obtain an average value in the QW layer of $\nu_{QW} \approx 0.22$. This is significantly lower than the established value for bulk silicon ($\nu_{bulk} \approx 0.278$), [40,41] and would correspond to a change in the elastic coefficients. Since a similar discrepancy is also observed for epitaxial Ge films [42], one cause of this smaller Poisson number may be that the elastic properties in the thin strained Si QW layer are different from those of bulk silicon. Moreover, we point out that the QW is under a strong compressive biaxial stress, with $\sigma_{xx} \approx \sigma_{yy} \approx -2.5$ GPa, as obtained from the measured strains using the elastic coefficients for silicon reported in Ref. [41] while rotating the stiffness tensor to match the orientation of our reference system [23]. Under these conditions, given the QW-layer thickness of about 10 nm, the Si material is at the critical point for the onset of plastic relaxation [43]. Therefore, nonlinear elastic effects may become relevant [44,45], causing an apparent deviation.

Furthermore, local isotropic compression or expansion may be triggered by the metallic gates. As a matter of fact, Eq. (5) relies on the assumption of zero surface normal stress ($\sigma_{zz} = 0$), a condition that may not be perfectly fulfilled in our case. In fact, the stiffness of the electrodes [23] and the local rotations of the lattice planes in the QW layer, relative to the sample surface, may lead a violation of this assumption [46]. These effects may combine into some amount of isotropic stress in the QW layer, locally changing the volume of the unit cell.

We point out that strain maps obtained with the same technique as that employed here were previously reported in Ref. [23], where a similar quantum structure has been investigated. However, in the device studied in Ref. [23], the quantum dots were fabricated starting from a Ge/Si$_{0.2}$Ge$_{0.8}$ material, which required the adoption of a plastically relaxed Ge virtual substrate. As a side effect of this choice, the measured strain maps provided evidence of the presence of long-range strain gradients, which were attributed to (1) the presence of the low-lying misfit-dislocation networks in the VS formed to accommodate the lattice mismatch, and (2) local fluctuations of Ge content in the Si$_{0.2}$Ge$_{0.8}$/Ge/Si VS [47]. In this heterostructure, their magnitude is smaller due to the lower mismatch between the Si substrate and the Si$_{0.66}$Ge$_{0.34}$ buffer layer, as well as the large thickness of the VS in the samples studied here (>5 μm in total). This is in agreement with the findings of Park *et al.*, who found that the strain fluctuations caused by the MD network formed during plastic relaxation in a

$Si_{0.7}Ge_{0.3}/Si/Si_{0.7}Ge_{0.3}/Si$ heterostructure were smaller in comparison with the electrode-induced strains [24,31].

In fact, it is difficult to distinguish the effect of the MD network and the larger TiN pads around the narrow clavier gates within the comparatively small field of view of the SXDM measurement. Thus, we study the effect of the MD network with μ-Raman shift mapping. The μ-Raman data, which are shown in the Supplemental Material [35], confirm that the magnitude of the corresponding modulation of the lattice strain is approximately 5×10^{-4}, but it takes place on a length scale larger than 1 μm, i.e., very long compared to the abrupt modulations induced by the clavier electrodes. We point also out that SXDM strain maps taken from the relaxed $Si_{0.66}Ge_{0.34}$ layers likewise confirm that the magnitude of the strain modulations due to the MD network is on the order of about a few 10^{-4}.

To evaluate the impact of the electrode-driven lattice deformation on the energy landscape, we determine, within the framework of deformation-potential theory, the strain-dependent conduction-band minimum in the Si QW layer [34], since it represents a key ingredient for the calculation of the eigenvalue spectrum of few-electron QD systems [48]. Due to the average tensile biaxial strain in the Si layer, the bottom of the conduction band in this region is controlled by the strain-induced fluctuation of the Δ_2 energy.

In Fig. 4, line profiles taken across five clavier electrodes along the y direction are shown for the strain components ε_{yy} (panel a) and ε_{zz} (panel b) measured in the QW layer at room temperature. The amplitudes of the electrode-driven strain fluctuations are, on average, larger by a factor of approximately 2 for high-stress sample A compared to low-stress sample B. This demonstrates that, even after lithography and structuring, the deposition of a high-stress TiN layer causes a stronger deformation in the underlying semiconductor compared to the TiN with weaker initial stress.

For what concerns the band edge, correspondingly, we observe that the Δ_2 energy (panel c) undergoes larger local modulations in sample A, for which we estimate a bandwidth of ± 4 meV to be compared with the range of ± 2 meV calculated for sample B. The maxima of the Δ_2 levels are located directly underneath the electrodes, while the minima are in the gap between them. Thus, without biasing the system, potential barriers of up to approximately 8 meV for sample A and approximately 4 meV for B are already present between the electrodes.

Tunnel-coupled QDs formed by periodic metal gates can be optimized to achieve low-variance Δ_{orb} of the orbital energy, E_{orb} (e.g., $E_{orb} \approx 3$ meV, $\Delta_{orb} \approx 0.2$ meV for an array of 9 QDs in Ref. [10]), suggesting the low impact of the strain potential. However, we suggest that several effects could increase the impact of the electrodes.

First, the strain modulations we observe for the TiN electrodes are much stronger compared with those we
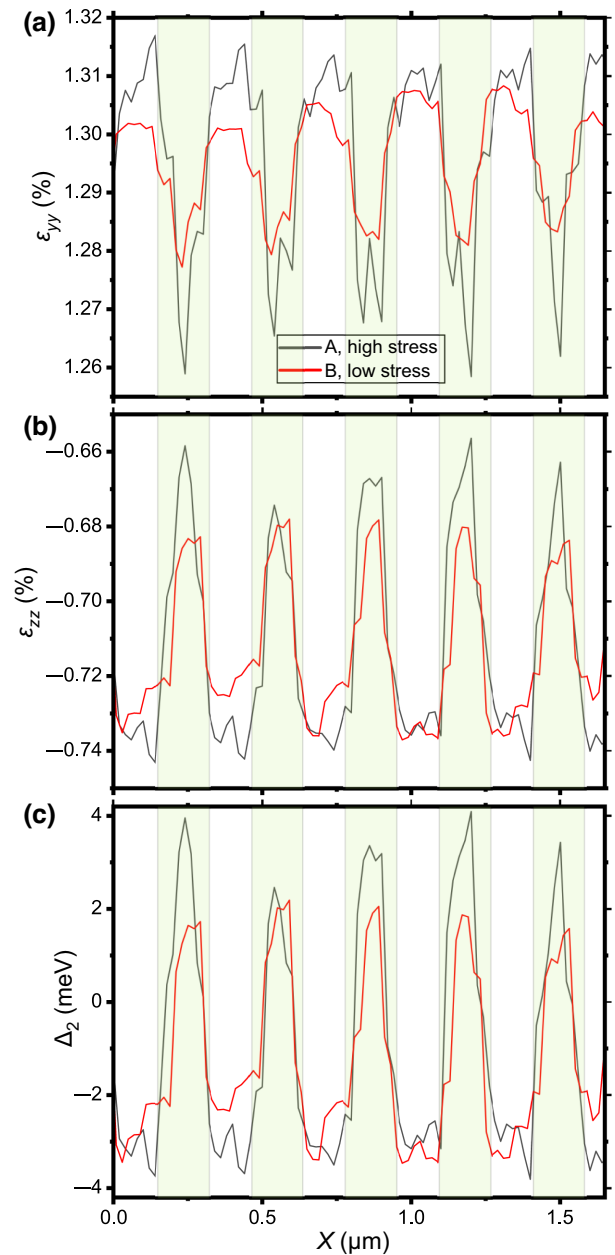

FIG. 4 Profiles across five clavier-gate electrodes of (a) in-plane strain ε_{yy}, (b) out-of-plane strain ε_{zz}, and (c) lower conduction-band-edge offset Δ_2. Extent of the electrodes is shaded in green.

previously measured in a device with metal (Ti/Pd, Al) electrodes [23]. This is due to the stronger stress (a few GPa) in TiN, compared with, e.g., Pd electrodes, which typically experience smaller stresses (<1 GPa) [49]. Thus, the impact of the TiN electrode studied here on the potential level of the band edge is larger than that of gate electrodes fabricated from metals such as Pd and Pt.

Second, the impact may be lowered by larger coverage, as usually at least two interleaved layers are used in quantum devices. Global strain will change the average level

of the band energy but not create barriers between the QDs in the qubus, which would obstruct shuttling. However, the coverage of the sample surface with gate material will not be complete, and the gate layers may be deposited at varying heights or with different processes. Thus, local modulations of the strain may still occur, even for devices with multiple gate layers.

We also highlight that the spatial periodicity of the strain follows the periodicity of the gates, and thus, that of the QDs. However, in a qubus device operated in conveyor mode, a QD adiabatically propagating has to be formed at all positions along the qubus. If gate biases are engineered without accounting for the unintentional barriers caused by the strain modulation and the amplitude of the shuttling pulse applied to the qubus is too small, the position of the electron may become undetermined during shuttling, in particular for TiN devices under high stress. We note that electron shuttling in a qubus device was shown with a typical QD confinement energy in Ref. [10], but there Pt electrodes were used and some signatures of tunneling were found during the conveyor-mode shuttle process [12]. Therefore, a tailored shaping of the periodic input signals of the shuttle device may be necessary to compensate for this effect.

To gain a better physical insight into the electrode-induced strain, we numerically assess the spatial distribution of the lattice deformation. To this aim, we model the heterostructure and the TiN electrodes with the solid mechanics module of the COMSOL Multiphysics suite to simulate the electrode-relaxation process through two-dimensional (2D) simulations based on the FEM.

It is well established that both the intrinsic stress, σ [28], and the Young's modulus, E, of sputtered TiN depend on the deposition parameters [50,51]. Since these quantities are required as input parameters for mechanical modeling, we preliminarily estimate the stress in the TiN electrodes from sample-curvature measurements by XRD as $\sigma_A = (-2.6 \pm 0.5)$ GPa and $\sigma_B = (-1.5 \pm 0.5)$ GPa and their Young's moduli by nanoindentation as $E_A = (106 \pm 25)$ GPa and $E_B = (91 \pm 19)$ GPa. As detailed in the Supplemental Material [35], we feed the FEM simulation with these data from sample A to calculate the deviations induced in the multilayer stack with respect to the average biaxial strain, which results from the relaxation of the TiN gates.

The Young's modulus of the CVD-grown SiO_2 layer separating the electrodes and the semiconductor layers is assumed from literature values [52]. It may vary for the ultrathin films studied here, depending on the deposition parameters with which the oxide is grown [53]. We note that, with regard to the strain distribution in the VS, the effect of increasing the stress in the TiN electrodes is similar to increasing the Young's modulus of SiO_2.

Our main results are summarized in Fig. 5, where we show the deviations of ε_{yy} and ε_{zz} from the average biaxial strain along the y-z plane, as calculated for a 1-μm-wide TiN contact pad (panels a and b) and for an array of clavier electrodes featuring a width of 160 nm and a pitch of 140 nm between them (panels c and d).

For the wide pad, we observe that the in-plane strain, shown in Fig. 5(a), is more positive underneath the center of the TiN slab, representing an expansion of the lattice along the in-plane direction, which propagates down to a depth of >200 nm below the sample surface. This behavior is in agreement with the positive in-plain strain modulation observed by SXDM in the Si QW layer under the wide (>1 μm) TiN pads. The modulation of ε_{zz} underneath the wide pad [Fig. 5(b)] is negative in the same region down to >100 nm below the surface, and thus, opposite in sign to ε_{yy}, as expected due to the Poisson effect and likewise observed underneath wide pads in the SXDM strain maps for the QW layer.

Also below the narrow clavier electrodes, down to a shallow depth of about 30 nm, the modulation of the in-plane strain, ε_{yy}, induced in the $Si_{0.66}Ge_{0.34}$ material [Fig. 5(c)] is positive, due to the downward propagation of the tensile deformation experienced by the gates once they partially release their initial compressive stress. However, deeper in the sample, we observe an inversion of the sign for ε_{yy} which becomes negative, resulting in a compression of the lattice along the in-plane direction. In other words, and quite surprisingly, directly underneath a narrow compressively stressed electrode, we observe a compressive modulation of ε_{yy}.

To qualitatively understand this counterintuitive effect, we observe that the tensile field from the bottom surface of the electrode propagates downward, mainly from its edges, and at an angle of about 45°, in line with numerical results reported in Ref. [54] for compressively strained $Si_{0.60}Ge_{0.40}$ stripes deposited on Si. On the other hand, the tensile field in the central electrode region does not propagate effectively downward. Consequently, starting from a certain depth, the central material region is sandwiched between two tensile strained domains; this induces its compressive distortion.

Having in mind this kind of phenomenology, we can better understand the SXDM strain maps, where we observe that, underneath the clavier electrodes, the modulations in ε_{yy} are negative (compressive) rather than positive (tensile). We therefore conclude that this depth-dependent strain inversion obtained by FEM may be the reason for the qualitative difference between the wide and narrow structures in the experimental data.

A similar inversion effect is also observed for the ε_{zz} strain component underneath the narrow electrodes, as shown in [Fig. 5(d)]. Indeed, at shallow depth, it is negative or close to zero underneath each clavier electrode, but
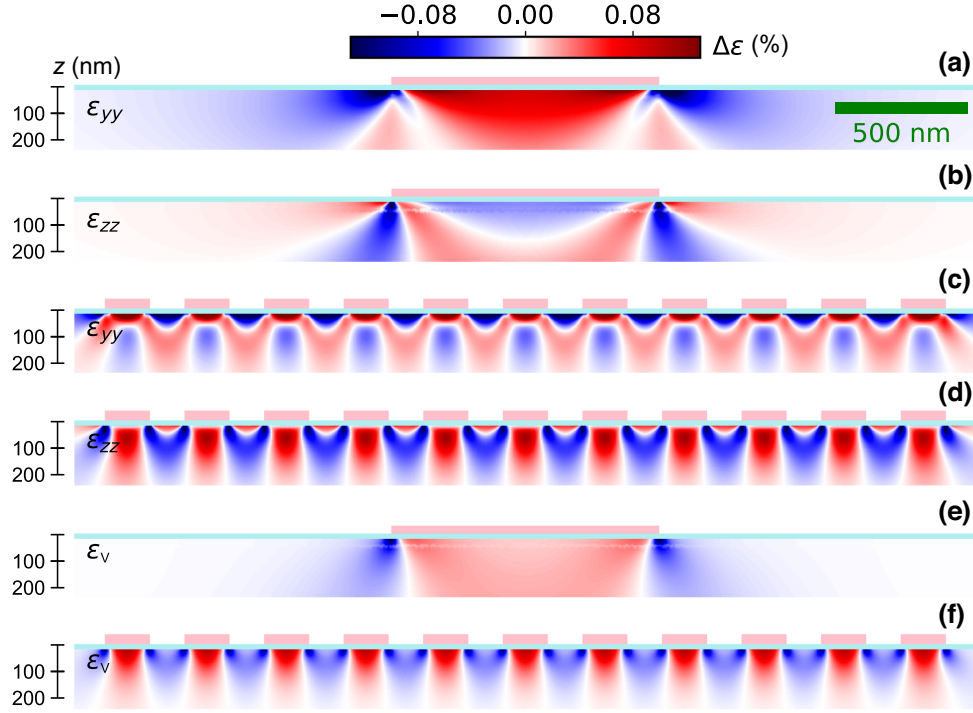
FIG. 5.   Simulated maps in the vertical y-z plane of the TiN-induced modulation of the diagonal strain components around the device structures. Maps around a TiN contact pad of 1 μm width of (a) ε_{yy} and (b) ε_{zz}. Maps of (c) ε_{yy} and (d) ε_{zz} around the qubus clavier region in sample A, featuring 160-nm-wide electrodes with 140-nm pitch. Maps of isotropic (hydrostatic) strain ε_V (e),(f). TiN electrodes are indicated by magenta bars; SiO$_2$ dielectric is the cyan layer. Scales and color bars are the same for all images.

becomes positive at larger depths, in line with the expected opposite behavior of ε_{yy} and ε_{zz}.

With the previously determined Poisson number, v, we calculate the local isotropic lattice constant, a_0, which is only affected by isotropic strain, according to [55]

$$a_0 = \frac{v(a+b) + (1-v)c}{(1+v)}. \tag{6}$$

With a_0, we determine the local isotropic (hydrostatic) strain, ε_V, by

$$\varepsilon_V = \frac{a_0}{a_{Si}} - 1 = \frac{v(a+b) + (1-v)c}{a_{Si}(1+v)} - 1, \tag{7}$$

which is plotted in Figs. 5(e) and 5(f) underneath the wide contact pad and the clavier electrode array, respectively. In both cases, we observe volume expansion underneath the compressively stressed electrodes, i.e., ε_V is positive. Both at the sides of the wide contact pad and between the narrow clavier electrodes, the volume strain is compressive and ε_V is negative. No change of sign at some depth occurs for the isotropic strain.

In the qubus, the electrons are shuttled horizontally within the Si QW, between the electrostatic QDs controlled by the clavier gates. To avoid potential barriers blocking

shuttling, we propose that extrema of the potential level of the Si conduction-band minimum should be avoided between the clavier electrodes. The FEM simulations in cross section demonstrate that the strain in the QW will depend on its distance from the sample surface. Therefore, to investigate the optimal depth at which the QW should be placed, we study horizontal line profiles of ε_{zz} across the simulated clavier electrodes, as shown in Fig. 6(a). They are taken as horizontal cuts from the simulated strain maps in cross section at four different depths from the sample surface. In Fig. 6(b), the corresponding profiles of the Δ_2 energy level are presented.

There is no depth at which the modulations of ε_{zz} and Δ_2 vanish along the horizontal profile. At each depth from $z = 25$ to 85 nm, they present a maximum beneath the center of each electrode. We consider this modulation of the Δ_2 level acceptable, since an energy offset within the electrostatic QDs can be accounted for by suitably tuning the voltage applied to the plunger gates, if the offset is similar for all QDs.

However, to avoid potential barriers between QDs during shuttling, we suggest that secondary Δ_2 modulations should be avoided between the clavier electrodes. In Fig. 6(b), for the curves taken at shallow depths, $z < 65$ nm, we observe secondary maxima in Δ_2 of a height of several meV at the midpoints between the electrodes. When
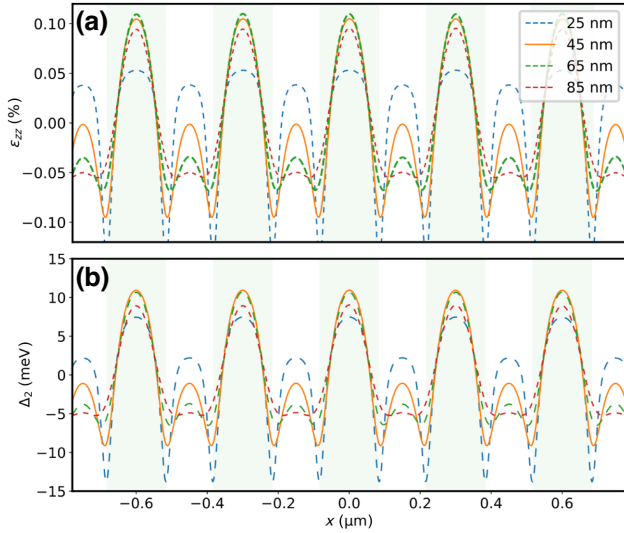
FIG. 6. Simulated profiles of (a) ε_{zz} and (b) the lower conduction-band-edge offset Δ_2 across five clavier-gate electrodes at different depths within the sample. Solid yellow line indicates the depth of the QW within the measured samples. Extent of the electrodes is shaded in green.

comparing the profiles at different depths, it is apparent that the amplitudes of these secondary maxima in Δ_2 decrease with depth. In particular, for $z = 85$ nm, they flatten out to a height of less than 1 meV, which is much smaller than the typical orbital energy of the QDs [10], and thus, not expected to obstruct coherent electron shuttling.

IV. DISCUSSION

Here, we investigated the effect of CMOS-processed TiN electrodes on the lateral-stain distribution in a 10-nm-thick Si QW. For several components of the strain tensor, local modulations of $2-8 \times 10^{-4}$ due to the stressing action of the TiN stripes were observed. By comparison of the global stress determined from the sample bowing in extended TiN films to the strain modulations caused by the small electrodes, we found that the macroscopic stress in the gate material was proportional to the microscopic strain induced by the electrodes. From band-structure calculations, we translated the electrode-driven strain modulations into local changes of the potential level of the conduction-band minimum with a bandwidth of several meV, similar to the orbital energy of an electrostatic QD hosting a few electrons [10]. These might act as unintentional barriers, hindering spin-coherent shuttling of electrons in conveyer mode [22], as well as affect charging energies and gate voltages required to operate spin qubits in large arrays [23,24].

We furthermore observed size effects of the electrode-induced strain modulations in the QW layer. From 2D FEM simulations, we found that, underneath a thin compressively stressed electrode, an inversion of the sign of

the strain occurred approximately 50 nm from the sample surface. This supported the experimental strain maps determined by SXDM, where we observed strain modulations of different signs underneath TiN stripes of 160 nm and >1-μm lateral extent, respectively.

Based on the simulation, QWs should be placed at a depth below 80 nm from the surface to avoid strain-induced potential barriers between the clavier electrodes studied here. However, simultaneously, the depth dependence of their electric field, voltage-pulse amplitudes applied to gates, and charging of a Si-capping layer need to be taken into account for the optimization of device performance. Moreover, we highlight that the optimal depth for the active layer with regard to strain depends on the device geometry, in particular, the width and spacing of the electrodes.

It is worth noting that, when cooled to typical operation temperatures in a quantum processor of approximately 20 mK, the strain landscape changes due to the different CTEs of all the materials in the sample.

We employed our FEM model for thermomechanical simulations, using literature values for the CTEs of TiN, SiO_2, $Si_{0.66}Ge_{0.34}$, and Si [56,57]. Simulated profiles of the strain, which are provided in the Supplemental Material [35], suggest that, by cooling the sample to <20 K, the amplitude of the electrode-induced strain modulations will decrease by about $1-2 \times 10^{-4}$. Albeit this thermal strain is rather small compared to the strain modulations we observed under standard condition, it needs to be taken into account when employing strain engineering to improve the device at its operating temperature.

We expect that a more detailed characterization of functional qubus devices will be required in the future. Moreover, we anticipate that similar modulations of the spatial landscapes of strain and potential occur in other technology platforms for quantum computing featuring micronscale lithographic structures. The impact of electrode-driven strain may be even more significant in metal-oxide-semiconductor-type devices, in which the quantum dots are located directly underneath the interface between the electrode and the oxide.

In summary, we demonstrate that strain induced in a thin Si QW layer by gate electrodes depends not only on the stress in the gate material, but also on the lateral dimensions of the electrodes and the depth of the QW layer in the sample. We predict that this effect is of a magnitude sufficient to affect the performance of quantum devices, such as coherent electron shuttles, but may be minimized by placing the QW layer at a suitable depth beneath the sample surface. Moreover, our results highlight the potential of SXDM as a structurally nonde-structive technique to study complex strain distributions in microscopic devices and to access important material-related information for microelectronics and quantum technology.

Raw data were generated at the ESRF Synchrotron Radiation Facility [63]. Derived data supporting the findings of this study are available from the corresponding authors upon reasonable request.

---

[1] C. E. Murray, A. Ying, S. M. Polvino, I. C. Noyan, M. Holt, and J. Maser, Nanoscale silicon-on-insulator deformation induced by stressed liner structures, J. Appl. Phys. **109**, 083543 (2011).

[2] T. Thorbeck and N. M. Zimmerman, Formation of strain-induced quantum dots in gated semiconductor nanostructures, AIP Adv. **5**, 087107 (2015).

[3] C. Y. Kang, R. Choi, M. Hussain, J. Wang, Y. J. Suh, H. C. Floresca, J. M. Kim, J. Kim, B. H. Lee, and R. Jammy, Effects of metal gate-induced strain on the performance of metal-oxide-semiconductor field effect transistors with titanium nitride gate electrode and hafnium oxide dielectric, Appl. Phys. Lett. **91**, 033511 (2018).

[4] S. Ito, H. Namba, T. Hirata, K. Ando, S. Koyama, N. Ikezawa, T. Suzuki, T. Saitoh, and T. Horiuchi, Effect of mechanical stress induced by etch-stop nitride: Impact on deep-submicron transistor performance, Microelectron. Reliab. **42**, 201 (2002).

[5] G. L. Bir and G. E. Pikus, *Symmetry and strain-induced effects in semiconductors* (Wiley, New York, 1974), vol. 484.

[6] M. Meyer, C. Déprez, T. R. van Abswoude, I. N. Meijer, D. Liu, C.-A. Wang, S. Karwal, S. Oosterhout, F. Borsoi, A. Sammak, N. W. Hendrickx, G. Scappucci, and M. Veldhorst, Electrical control of uniformity in quantum dot devices, Nano Lett. **23**, 2522 (2023).

[7] W. Ha, S. D. Ha, M. D. Choi, Y. Tang, A. E. Schmitz, M. P. Levendorf, K. Lee, J. M. Chappell, T. S. Adams, D. R. Hulbert, E. Acuna, R. S. Noah, J. W. Matten, M. P. Jura, J. A. Wright, M. T. Rakher, and M. G. Borselli, A flexible design platform for Si/SiGe exchange-only qubits with low disorder, Nano Lett. **22**, 1443 (2021).

[8] A. M. J. Zwerver, T. Krähenmann, T. F. Watson, L. Lampert, H. C. George, R. Pillarisetty, S. A. Bojarski, P. Amin, S. V. Amitonov, J. M. Boter, R. Caudillo, D. Correas-Serrano, J. P. Dehollain, G. Droulers, E. M. Henry, *et al.*, Qubits made by advanced semiconductor manufacturing, Nat. Electron. **5**, 184 (2022).

[9] M. F. Gonzalez-Zalba, S. de Franceschi, E. Charbon, T. Meunier, M. Vinet, and A. S. Dzurak, Scaling silicon-based quantum computing using CMOS technology, Nat. Electron. **4**, 872 (2021).

[10] D. M. Zajac, T. M. Hazard, X. Mi, E. Nielsen, and J. R. Petta, Scalable Gate Architecture for a One-Dimensional Array of Semiconductor Spin Qubits, Phys. Rev. Appl. **6**, 054013 (2016).

[11] N. W. Hendrickx, W. I. L. Lawrie, L. Petit, A. Sammak, G. Scappucci, and M. Veldhorst, A single-hole spin qubit, Nat. Commun. **11**, 1 (2020).

[12] I. Seidler, T. Struck, R. Xue, N. Focke, S. Trellenkamp, H. Bluhm, and L. R. Schreiber, Conveyor-mode single-electron shuttling in Si/SiGe for a scalable quantum computing architecture, npj Quantum Inf. **8**, 1 (2022).

[13] T. G. Dziura, B. Bunday, C. Smith, M. M. Hussain, R. Harris, X. Zhang, and J. M. Price, in *Metrology, Inspection, and Process Control for Microlithography XXII* (2008).

[14] F. Fillot, T. Morel, S. Minoret, I. Matko, S. Maîtrejean, B. Guillaumot, B. Chenevier, and T. Billon, Investigations of titanium nitride as metal gate material, elaborated by metal organic atomic layer deposition using TDMAT and NH$_3$, Microelectron. Eng. **82**, 248 (2005).

[15] J. Musschoot, Q. Xie, D. Deduytsche, S. V. den Berghe, R. L. V. Meirhaeghe, and C. Detavernier, Atomic layer

deposition of titanium nitride from TDMAT precursor, Microelectron. Eng. **86**, 72 (2009).

[16] E. T. Campbell, B. M. Terhal, and C. Vuillot, Roads towards fault-tolerant universal quantum computation, Nature **549**, 172 (2017).

[17] L. R. Schreiber and H. Bluhm, Toward a silicon-based quantum computer, Science **359**, 393 (2018).

[18] A. Chatterjee, P. Stevenson, S. De Franceschi, A. Morello, N. P. de Leon, and F. Kuemmeth, Semiconductor qubits in practice, Nat. Rev. Phys. **3**, 157 (2021).

[19] S. G. J. Philips, M. T. Mądzik, S. V. Amitonov, S. L. de Snoo, M. Russ, N. Kalhor, C. Volk, W. I. L. Lawrie, D. Brousse, L. Tryputen, B. P. Wuetz, A. Sammak, M. Veldhorst, G. Scappucci, and L. M. K. Vandersypen, Universal control of a six-qubit quantum processor in silicon, Nature **609**, 919 (2022).

[20] J. Yoneda, W. Huang, M. Feng, C. H. Yang, K. W. Chan, T. Tanttu, W. Gilbert, R. C. C. Leon, F. E. Hudson, K. M. Itoh, A. Morello, S. D. Bartlett, A. Laucht, A. Saraiva, and A. S. Dzurak, Coherent spin qubit transport in silicon, Nat. Commun. **12**, 1 (2021).

[21] J. M. Boter, J. P. Dehollain, J. P. G. van Dijk, Y. Xu, T. Hensgens, R. Versluis, H. W. L. Naus, J. S. Clarke, M. Veldhorst, F. Sebastiano, and L. M. K. Vandersypen, Spiderweb Array: A Sparse Spin-Qubit Array, Phys. Rev. Appl. **18**, 024053 (2022).

[22] V. Langrock, J. A. Krzywda, N. Focke, I. Seidler, L. R. Schreiber, and Ł Cywinski, Blueprint of a Scalable Spin Qubit Shuttle Device for Coherent Mid-Range Qubit Transfer in Disordered Si/SiGe/SiO₂, PRX Quantum **4**, 020305 (2023).

[23] C. Corley-Wiciak, C. Richter, M. H. Zoellner, I. Zaitev, C. Manganelli, E. Zatterin, T. Schülli, A. A. Corley-Wiciak, J. Katzer, F. Reichmann, W. M. Klesse, N. W. Hendrickx, A. Sammak, M. Veldhorst, G. Scappucci, M. Virgilio, and G. Capellini, Nanoscale mapping of the 3D strain tensor in a germanium quantum well hosting a functional spin qubit device, ACS Appl. Mater. Interfaces **15**, 3119 (2023).

[24] J. Park, Y. Ahn, J. A. Tilka, K. C. Sampson, D. E. Savage, J. R. Prance, C. B. Simmons, M. G. Lagally, S. N. Coppersmith, M. A. Eriksson, M. V. Holt, and P. G. Evans, Electrode-stress-induced nanoscale disorder in Si quantum electronic devices, APL Mater. **4**, 066102 (2016).

[25] M. Ohring, in *Materials Science of Thin Films*, 2nd ed., edited by M. Ohring (Academic Press, San Diego, 2002), pp. 711–781.

[26] S. Ohya, *et al.*, Room temperature deposition of sputtered TiN films for superconducting coplanar waveguide resonators, Supercond. Sci. Technol. **27**, 015009 (2013).

[27] M. Nahar, N. Rocklein, M. Andreas, G. Funston, and D. Goodner, Stress modulation of titanium nitride thin films deposited using atomic layer deposition, J. Vac. Sci. Technol., A **35**, 01B144 (2017).

[28] M. M. Hussain, M. A. Quevedo-Lopez, H. N. Alshareef, D. Larison, K. Mathur, and B. E. Gnade, Deposition method-induced stress effect on ultrathin titanium nitride etch characteristics, Electrochem. Solid-State Lett. **9**, G361 (2006).

[29] G. C. A. M. Janssen, M. M. Abdalla, F. Van Keulen, B. R. Pujada, and B. Van Venrooy, Celebrating the 100th anniversary of the Stoney equation for film stress: Developments from polycrystalline steel strips to single crystal silicon wafers, Thin Solid Films **517**, 1858 (2009).

[30] N. D'Anna, D. Ferreira Sanchez, G. Matmon, J. Bragg, P. C. Constantinou, T. J. Z. Stock, S. Fearn, S. R. Schofield, N. J. Curson, M. Bartkowiak, Y. Soh, D. Grolimund, S. Gerber, and G. Aeppli, Non-destructive x-ray imaging of patterned delta-layer devices in silicon, Adv. Electron. Mater. **9**, 2201212 (2023).

[31] P. G. Evans, D. E. Savage, J. R. Prance, C. B. Simmons, M. G. Lagally, S. N. Coppersmith, M. A. Eriksson, and T. U. Schülli, Nanoscale distortions of Si quantum wells in Si/SiGe quantum-electronic heterostructures, Adv. Mater. **24**, 5217 (2012).

[32] G. A. Chahine, M.-I. Richard, R. A. Homs-Regojo, T. N. Tran-Caliste, D. Carbone, V. L. R. Jacques, R. Grifone, P. Boesecke, J. Katzer, I. Costina, H. Djazouli, T. Schroeder, and S. T. U, Imaging of strain and lattice orientation by quick scanning x-ray microscopy combined with three-dimensional reciprocal space mapping, J. Appl. Crystallogr. **47**, 762 (2014).

[33] S. J. Leake, G. A. Chahine, H. Djazouli, T. Zhou, C. Richter, J. Hilhorst, L. Petit, M.-I. Richard, C. Morawe, R. Barrett, L. Zhang, R. A. Homs-Regojo, V. Favre-Nicolin, P. Boesecke, and T. U. Schülli, The nanodiffraction beamline ID01/ESRF: A microscope for imaging strain and structure, J. Synchrotron Radiat. **26**, 571 (2019).

[34] C. G. Van de Walle, Band lineups and deformation potentials in the model-solid theory, Phys. Rev. B **39**, 1871 (1989).

[35] See the Supplemental Material at http://link.aps.org/supplemental/10.1103/PhysRevApplied.20.024056 for a description of the synchrotron data analysis, maps of lattice strain and composition in the $Si_{0.66}Ge_{0.34}$ buffer layer, additional results from Raman microspectroscopy strain mapping, nanoindentation measurements and film stress measurement by sample curvature, details of FEM simulations and band-structure calculations, strain and band-energy profiles at low temperature, and ptychographic reconstruction of the x-ray nanoprobe. It also contains Refs. [58–62].

[36] V. Favre-Nicolin, G. Girard, S. Leake, J. Carnis, Y. Chushkin, J. Kieffer, P. Paleo, and M.-I. Richard, PyNX: High-performance computing toolkit for coherent x-ray imaging based on operators, J. Appl. Crystallogr. **53**, 1404 (2020).

[37] A. Rack, Hard x-ray imaging at ESRF: Exploiting contrast and coherence with the new EBS storage ring, Synchrotron Radiat. News **33**, 20 (2020).

[38] C. Richter, V. M. Kaganer, A. Even, A. Dussaigne, P. Ferret, F. Barbier, Y.-M. Le Vaillant, and T. U. Schülli, Nanoscale Mapping of the Full Strain Tensor, Rotation, and Composition in Partially Relaxed $In_xGa_{1-x}N$ Layers by Scanning X-Ray Diffraction Microscopy, Phys. Rev. Appl. **18**, 064015 (2022).

[39] J. L. Schlenker, G. V. Gibbs, and J. M. B. Boisen, Strain-tensor components expressed in terms of lattice parameters, Acta Cryst. **A34**, 52 (1978).

[40] J. P. Dismukes, L. Ekstrom, and R. J. Pfaff, Lattice parameter and density in germanium-silicon alloys, J. Phys. Chem. **68**, 3021 (1964).

[41] J. J. Wortman and R. A. Evans, Young's modulus, shear modulus, and Poisson's ratio in silicon and germanium, J. Appl. Phys. **36**, 153 (1965).

[42] J. Bharathan, J. Narayan, G. Rozgonyi, and G. E. Bulman, Poisson ratio of epitaxial germanium films grown on silicon, J. Electron. Mater. **42**, 40 (2013).

[43] Y. Liu, K.-P. Gradwohl, C.-H. Lu, T. Remmele, Y. Yamamoto, M. H. Zoellner, T. Schroeder, T. Boeck, H. Amari, C. Richter, and M. Albrecht, Role of critical thickness in SiGe/Si/SiGe heterostructure design for qubits, J. Appl. Phys. **132**, 085302 (2022).

[44] C. Wang, J. Gu, X. Kuang, and S. Xiang, Equation of state, nonlinear elastic response, and anharmonic properties of diamond-cubic silicon and germanium: First-principles investigation, Z. Naturforsch. A **70**, 403 (2015).

[45] S. H. B. Bosher and D. J. Dunstan, Effective elastic constants in nonlinear elasticity, J. Appl. Phys. **97**, 103505 (2005).

[46] A. E. Romanov, T. J. Baker, S. Nakamura, J. S. Speck, and E. U. C. S. B. Group, Strain-induced polarization in wurtzite III-nitride semipolar layers, J. Appl. Phys. **100**, 023522 (2006).

[47] M. H. Zoellner, M.-I. Richard, G. A. Chahine, P. Zaumseil, C. Reich, G. Capellini, F. Montalenti, A. Marzegalli, Y.-H. Xie, T. U. Schülli, M. Häberlen, P. Storck, and T. Schroeder, Imaging structure and composition homogeneity of 300 mm SiGe virtual substrates for advanced CMOS applications by scanning x-ray diffraction microscopy, ACS Appl. Mater. Interfaces **7**, 9031 (2015).

[48] C. R. Anderson, M. F. Gyure, S. Quinn, A. Pan, R. S. Ross, and A. A. Kiselev, High-precision real-space simulation of electrostatically confined few-electron states, AIP Adv. **12**, 065123 (2022).

[49] F. Afshar, S. Nazarpour, and A. Cirera, Survey of the theory and experimental measurements of residual stress in Pd thin film, J. Appl. Phys. **108**, 093513 (2010).

[50] P. Patsalas, C. Charitidis, and S. Logothetidis, The effect of substrate temperature and biasing on the mechanical properties and structure of sputtered titanium nitride thin films, Surf. Coat. Technol. **125**, 335 (2000).

[51] T. Namazu, S. Inoue, H. Takemoto, and K. Koterazawa, Mechanical properties of polycrystalline titanium nitride films measured by XRD tensile testing, IEEJ Trans. Sens. Micromachines **125**, 374 (2005).

[52] M. T. Kim, Influence of substrates on the elastic reaction of films for the microindentation tests, Thin Solid Films **283**, 12 (1996).

[53] Y.-J. Su, C.-F. Qian, M.-H. Zhao, and T.-Y. Zhang, Microbridge testing of silicon oxide/silicon nitride bilayer films deposited on silicon wafers, Acta Mater. **48**, 4901 (2000).

[54] E. Bonera, M. Bollani, D. Chrastina, F. Pezzoli, A. Picco, O. G. Schmidt, and D. Terziotti, Substrate strain manipulation by nanostructure perimeter forces, J. Appl. Phys. **113**, 164308 (2013).

[55] A. P. Boresi and R. J. Schmidt, *Advanced mechanics of materials* (John Wiley & Sons, New York, 2002).

[56] Y. S. Touloukian, R. K. Kirky, R. E. Taylor, T. Y. R. Lee, *et al.*, *Thermal properties of matter, TPRC data books* (Plenum Press, New York, 1975), Vol. 13.

[57] F. Schaffler, *Properties of Advanced Semiconductor Materials GaN, AlN, InN, BN, SiC, SiGe* (John Wiley & Sons, New York, 2001), pp. 149–188.

[58] L. Becker, P. Storck, T. Schulz, M. H. Zoellner, L. Di Gaspare, F. Rovaris, A. Marzegalli, F. Montalenti, M. De Seta, G. Capellini, G. Schwalb, T. Schroeder, and M. Albrecht, Controlling the relaxation mechanism of low strain $Si_{1-x}Ge_x$/Si(001) layers and reducing the threading dislocation density by providing a preexisting dislocation source, J. Appl. Phys. **128**, 215305 (2020).

[59] G. Capellini, M. De Seta, P. Zaumseil, G. Kozlowski, and T. Schroeder, High temperature x ray diffraction measurements on Ge/Si (001) heterostructures: A study on the residual tensile strain, J. Appl. Phys. **111**, 073518 (2012).

[60] C. A. Clifford and M. P. Seah, Modelling of nanomechanical nanoindentation measurements using an AFM or nanoindenter for compliant layers on stiffer substrates, Nanotechnology **17**, 5283 (2006).

[61] C. A. Klein and G. F. Cardinale, Young's modulus and Poisson's ratio of CVD diamond, Diamond Relat. Mater. **2**, 918 (1993).

[62] C. L. Manganelli, M. Virgilio, O. Skibitzki, M. Salvalaglio, D. Spirito, P. Zaumseil, Y. Yamamoto, M. Montanari, W. M. Klesse, and G. Capellini, Temperature dependence of strain–phonon coefficient in epitaxial Ge/Si (001): A comprehensive analysis, J. Raman Spectrosc. **51**, 989 (2020).

[63] https://doi.org/10.15151/ESRF-ES-446319034.